Direct Measurement of the Return Current Instability in a Laser-Produced Plasma

A. L. Milder,[1,2,3,*] J. Zielinski,[3] J. Katz,[1] W. Rozmus,[3] D. Edgell,[1] A. Hansen,[1] M. Sherlock,[4] C. Bruulsema,[3] J. P. Palastro,[1] D. Turnbull,[1] and D. H. Froula[1,2]

[1]*Laboratory for Laser Energetics, 250 East River Road, Rochester, New York 14623, USA*
[2]*Department of Physics and Astronomy, University of Rochester, Rochester, New York 14623, USA*
[3]*Department of Physics, University of Alberta, Edmonton, Alberta T6G 2E1, Canada*
[4]*Lawrence Livermore National Laboratory, 7000 East Avenue, Livermore, California 94550, USA*

(Received 22 June 2022; revised 22 July 2022; accepted 11 August 2022; published 8 September 2022)

Measurements were made of the return current instability growth rate, demonstrating its concurrence with nonlocal transport. Thomson scattering was used to measure a maximum growth rate of 5.1×10^9 Hz, which was 3 times less than classical Spitzer-Härm theory predicts. The measured plasma conditions indicate the heat flux was nonlocal, and Vlasov–Fokker-Planck simulations that account for nonlocality reproduce the measured growth rates. Furthermore, the threshold for the return current instability was measured ($\delta_T = 0.017 \pm 0.002$) to be in good agreement with previous theoretical models.

DOI: 10.1103/PhysRevLett.129.115002

Significant progress has been made in understanding laboratory and astrophysical plasmas through the use of fluid approximations [1–3], but recently an increasing amount of work has been dedicated to understanding the kinetic effects and how the microscale physics impacts the larger macroscopic systems. Some of the physics under investigation includes: non-Maxwellian distribution functions [4–6], fast ion populations [7,8], nonlocal thermal transport [9,10], and transport driven instabilities [11]. In laser-produced plasmas, much of the recent progress in elucidating the role of kinetic effects has been achieved with Thomson scattering, showing non-Maxwellian distribution functions [4–6], nonlocal heat flux [12,13], and kinetic evolution of instabilities [14–17].

In particular, kinetic effects associated with nonlocal transport have impacted the interpretation of inertial confinement fusion implosions, laboratory astrophysics, and high-energy density experiments. Understanding of transport and transport driven instabilities often starts with the classical theories of Spitzer and Härm [18] or Braginskii [19]. However, when the Knudsen number (δ_T), the ratio of the electron-ion mean free path (λ_{ei}) to the temperature gradient scale length ($L_T = |\nabla \ln Te|^{-1}$), is larger than $\sim 10^{-2}$ accurate modeling requires semianalytic nonlocal closure relations in hydrodynamic models [20–24] or a kinetic approach based on numerical solutions to the Fokker-Planck equation [9,10,25–27]. Historically, challenges in accounting for kinetic effects, particularly in heat transport, have been addressed with *ad hoc* corrections to the Spitzer-Härm theory [28–30] in order to match experimental observables.

In a plasma, heat carrying electrons travel down the temperature gradient (q_{flux}), generating a neutralizing return current (j_{return}) consisting of slower counterpropagating electrons. Heat carrying electrons have a velocity around 3 times the electron thermal velocity resulting in coupling mainly with electron plasma waves while the return current consists of electrons around the electron thermal velocity. When the return current is large enough to shift the peak of the electron distribution function beyond the phase velocity of the ion acoustic waves, the slope of the distribution function becomes inverted, and the electrons transfer energy to the waves (inverse Landau damping). These transport driven waves become absolutely unstable when the inverse Landau damping rate exceeds the ion damping rate [3]. This return current instability (RCI) is predicted to drive a broad turbulent spectrum of ion acoustic waves that limit the return current, inhibit heat transport [31–34], modify laser absorption [35,36], and alter the fluctuation spectrum from which other ion instabilities grow [37–39]. Previous experimental work has shown anomalous absorption linked to ion turbulence [35] and evidence of reduced heat flux [33].

In this Letter, we present the first measurements of the threshold and linear growth rate of the return current instability driven by electron heat flux. The thorough characterization of the plasma conditions shows that the return current instability occurs concurrently with nonlocal transport. Thomson scattering was used to measure a maximum RCI growth rate of 5.1×10^9 Hz, which was 3 times less than classical Spitzer-Härm theory predicts, but the RCI threshold was measured ($\delta_T = 0.017 \pm 0.002$) to be in good agreement with previous theoretical models [31,38]. Measured plasma conditions indicate that the heat flux was nonlocal and electron velocity distribution functions from Vlasov–Fokker-Planck (VFP) simulations, which treat this nonlocality kinetically, reproduce the measured growth rates. These experiments provide a thorough description of the plasma conditions and the

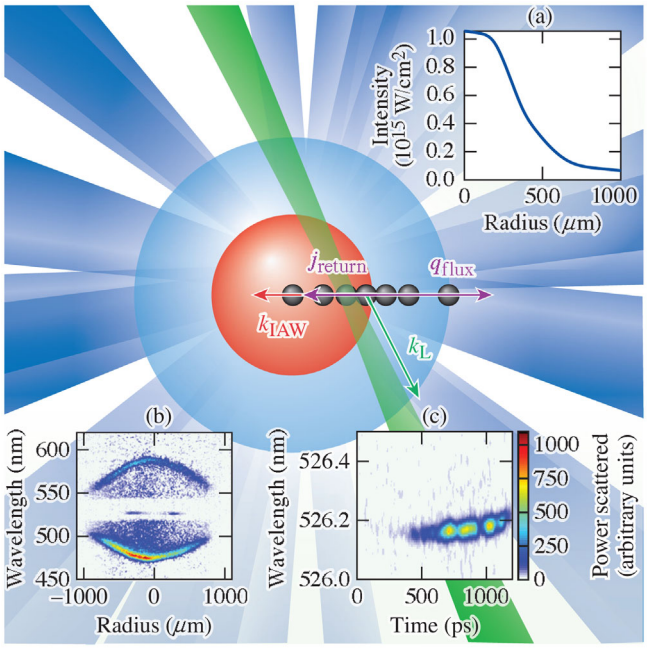

FIG. 1. Ultraviolet beams (blue) were used to heat the plasma, and a 526.5-nm beam (green) was used as a Thomson-scattering probe. This heating configuration produced a hot region (red sphere) surrounded by a cooler region of plasma (blue sphere). Over a series of shots, the Thomson-scattered light was collected at different locations (black spheres). The ion-acoustic waves (k_{IAW}, red arrow) probed by Thomson scattering were aligned with the heat flux and return current (purple arrows). The insets show (a) the overlapped heater beam intensity, (b) the spatially resolved electron-plasma wave features measured when the probe beam passed through the center of the plasma, and an example of (c) the temporally resolved blueshifted ion acoustic wave that was driven by RCI ($r = 475$ μm).

associated return current instability, which enabled a detailed comparison with theory and simulations and can now be used to better understand the impact of return current instability in laboratory and astrophysical plasmas.

Figure 1 shows the experimental configurations where a supersonic Mach 3 gas jet (not shown) with an exit diameter of 2 mm produced a gas plume of argon. Eleven 351-nm ultraviolet beams of the OMEGA laser system [40] were focused 2 mm above the nozzle to heat the plasma. Each beam delivered 200 J in a 1-ns duration full-width at half-maximum (FWHM) flat-top pulse. The beams used distributed phase plates, polarization smoothing, and smoothing by spectral dispersion and achieved a peak overlapped intensity of $I_{\mathrm{UV}}^{\mathrm{total}} = 1.1 \times 10^{15}$ W/cm^2 [Fig. 1(a)].

The overlapped beams produced a hot region of plasma surrounded by a colder region. The overlapped intensity profile [Fig. 1(a)] created an electron temperature gradient that drove "fast" electrons from the hot region to the cold region. In order to maintain an absolute calibration in the Thomson-scattering power between each shot, the Thomson-scattered light was collected from various radial locations in the plasma by moving the heater beams and gas jet. The configuration maintained the probed ion-acoustic wave vector parallel to the direction of the heat flux (Fig. 1). A distributed phase plate was used on the Thomson-scattering probe beam ($\lambda_0 = 526.5$ nm) to produce a 200-μm FWHM flat-top focal spot. This beam was used with ~4 J in a 300-ps FWHM flat-top pulse ($I_{2\omega} = 4.2 \times 10^{13}$ W/cm^2) delayed 700 ps from the start of the heater beams to measure spatially resolved Thomson scattering [Fig. 1(b)] or with ~5 J in a 2-ns FWHM flat-top pulse, cotimed with the beginning of the heating beams, and a 100-μm phase plate ($I_{2\omega} = 3.2 \times 10^{13}$ W/cm^2) to measure temporally resolved Thomson scattering [Fig. 1(c)]. The Thomson-scattering diagnostic, both temporally resolved and spatially resolved, collects light with a 60° scattering angle.

Figure 1(b) shows spatially resolved electron plasma waves that were used to measure the electron temperature and density profiles. A 15-nm-wide dielectric notch filter, centered at 527 nm, suppressed the ion acoustic wave features by 4 orders of magnitude. The ion acoustic and electron plasma wave features can be distinguished by their wavelength shifts allowing only the ion-acoustic wave to be suppressed. The RCI driven ion-acoustic wave signal can be seen through the filter at approximately ± 350 μm. The Thomson-scattering system used a 0.3-m spectrometer with a 150 grooves/mm grating to achieve a spectral resolution of 1.4 nm. Light was collected from a volume 65 μm × 200 μm with a spatial resolution of 20 μm along the propagation direction of the probe [41].

Figure 1(c) shows the temporally resolved ion-acoustic waves measured at a radius of $r = 475$ μm from the center of the gas jet. Light was collected from a volume 25 × 25 × 100 μm (87 × 87 × 100 μm for time resolved electron plasma waves). Only the blueshifted ion-acoustic wave is visible in the spectrum as it is enhanced by the return current while the redshifted wave is suppressed; the return current provides additional landau damping to waves counterpropagating with respect to the return current. The Thomson-scattering system used a 1-m spectrometer with a 2160 grooves/mm grating to resolve the ion-acoustic wave shifts (spectral resolution of 0.023 nm) [42]. The grating was masked to allow the system to maintain the spectral resolution while providing 20 ps FWHM temporal resolution [43].

Figure 2(a) displays the electron density and electron temperature as a function of time at the center of the plasma ($r = 0$ μm). These plasma conditions were determined from the temporally resolved electron-plasma wave features using the standard collisionless spectral density function modified to allow for super-Gaussian electron velocity distribution functions [4,44]. Over the first 500 ps, the temperature and density increased as the plasma was

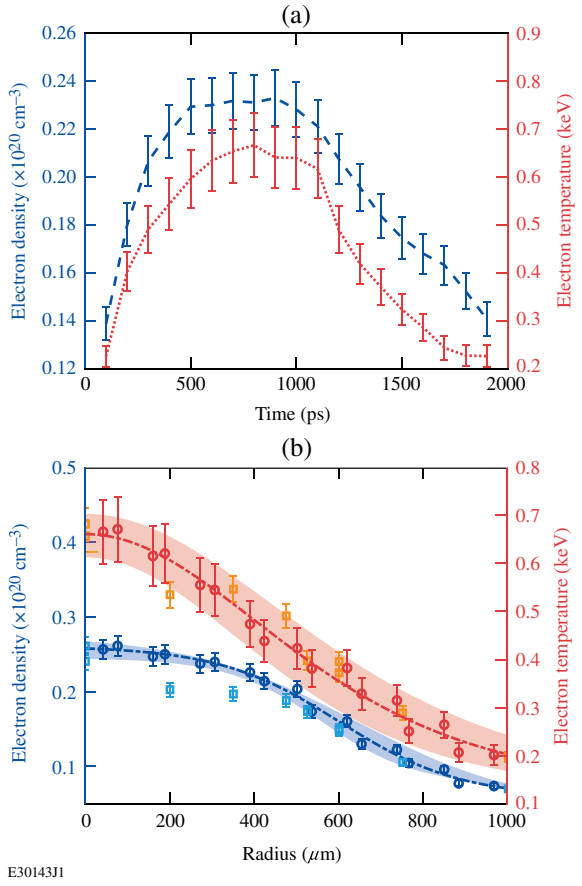

FIG. 2. Electron density, blue left axes, and electron temperature, red right axes, as a function of (a) time and (b) radius. Error bars give the uncertainty in the measured plasma conditions. (b) The data were matched with a hyperbolic tangent (dashed curves) to provide continuous functions for calculating the Knudsen number. The shaded regions mark the 90% confidence interval for these fits. Dark red and blue data (circles) were measured in a single spatially resolved spectrum, while the lighter color data (squares) represent the set of temporally resolved spectra taken at different radii over multiple shots.

ionized and heated through inverse bremsstrahlung heating. The plasma conditions were quasistationary over the following 500 ps. At 1 ns, the heating beams turned off, and the plasma cooled and relaxed. Temporally resolved plasma conditions were used to determine the temporal gradients and identify the quasistationary region for imaging Thomson-scattering measurements, which were made from 700 to 1000 ps.

Figure 2(b) shows the spatially resolved electron density and electron temperature profiles that both decrease as a function of radius. Good agreement was obtained between the data from a single spatially resolved dataset and ten temporally resolved datasets. Small variations were observed in the plasma conditions due to variations in the laser drive and initial gas density.

Figure 3 shows the measured temporally resolved ion-acoustic wave amplitudes while the plasma conditions were quasistationary (500–1000 ps). At 475 μm [Fig. 3(a)], the ion acoustic wave grows as a function of time consistent with the return current instability. This is further supported by comparison with growth rate calculations from the Spitzer-Härm theory and from VFP simulations. The growth rate in the Spitzer-Härm theory was found to be significantly larger than observed in the plasma, which is attributed to the nonlocality of the heat transport. VFP simulations, which include these effects kinetically, show excellent agreement with the data. At a radius of 200 μm [Fig. 3(b)], the ion acoustic wave decays as a function of time indicating that the plasma was stable to the return current instability. The ion-acoustic wave was driven above the thermal fluctuation level at early time, likely by transient RCI or ponderomotive and thermal effects as the plasma was being formed. As such, these negative growth rates only serve to show the plasma is stable to the RCI.

Figure 3(c) compares the ion-acoustic growth rates from simulation and experiment as a function of space. As with the case at 475 μm, the Spitzer-Härm theory overpredicts the growth rate at all spatial locations. Nonlocal transport, included in VFP, was needed to match the measured growth rates. The experiment and simulation showed the return current instability occurred over a large spatial extent from ~300 to 1000 μm but is maximized around 600 μm where the temperature gradient is large. This association with the temperature gradient helps identify this instability as a transport driven instability. Simulations predicted the instability threshold was crossed around 200 μm, while experimental data show the threshold between 200 μm and 350 μm.

Vlasov–Fokker-Planck simulations were performed with the code *K*2 [45], which was operated with 1 spatial dimension (r) and 3 velocity dimensions (1D3V). The code uses a Legendre expansion to represent the electron distribution function as the sum of an isotropic component $f_0(v,r,t)$ and first-order Legendre mode $f_1(v,r,t)$ via $f = f_0(v,r,t) + f_1(v,r,t)\cos\theta$, with θ being the angle between the velocity vector and the spatial coordinate. *K*2 applies the nonlinear electron-electron Fokker-Planck collision operator to f_0, and accounts for the effect of electron-ion angular scattering on f_1, in addition to terms describing inverse bremsstrahlung heating, thermal transport, the self-consistent electric field, and associated return current [45]. In the simulations, the plasma density was set to the experimental values (ion motion was ignored), and the plasma was heated with the experimental intensity profile [Fig. 1(a)]. This mostly reproduced the temperature profile seen in the experiments, but with a small error that was attributed to radiative cooling. To account for this error, a small amount of radiative cooling was applied to the simulations [46], which was slowly adjusted until the simulated temperature agreed with the experimental profile to within 0.4%. This technique does not significantly alter

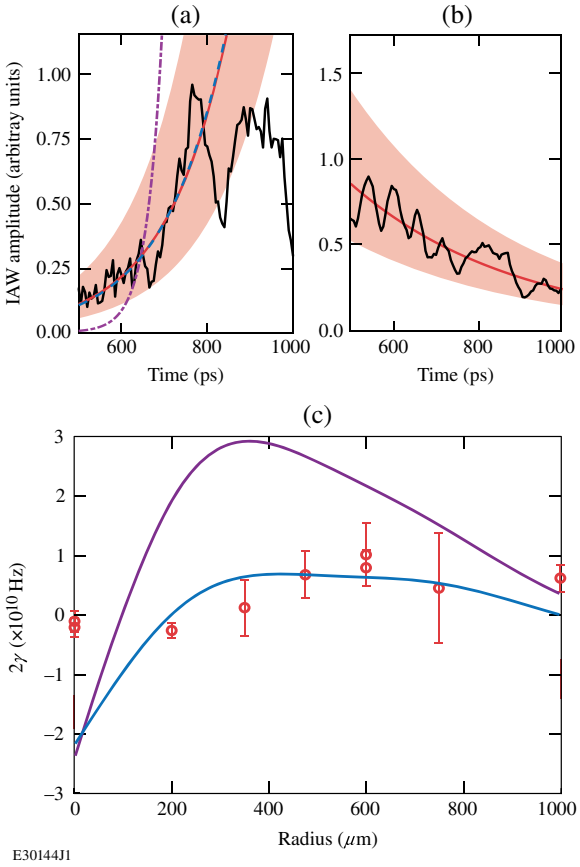

FIG. 3. The ion acoustic wave amplitude (black) at a radius of (a) 475 μm and (b) 200 μm are matched with an exponential model (red curve) with a shaded 90% confidence interval. (a) Exponential models with growth rates from the Spitzer-Härm theory (purple) and VFP simulations (blue) are compared to the data. (c) Measured growth rates (red) are compared to growth rates from the Spitzer-Härm theory (purple) and VFP simulations (blue) as a function of radius.

the character of the distribution function, but rather acts to maintain better consistency between the simulation and experiment [12]. The ionization state was set using FLYCHK ($Z \sim 12$–16) with the experimental plasma conditions. An equilibrium was reached after a few collision times, and the simulated $f_0(v)$ developed a super-Gaussian order of up to 3 near the center of the plasma in agreement with measurements.

The resulting distribution function calculated by $K2$ was used to determine the growth rate of the unstable ion-acoustic waves in the limit of small ion acoustic damping, valid in this wave vector regime:

$$\gamma = \pi^2 \frac{\omega_r^3}{\omega_{pi}^2} \frac{\omega_{pe}^2}{k^2} \left[-\frac{\omega_r}{k} f_0(0) + \cos\theta \int_0^\infty f_1(v) dv \right] \qquad (1)$$

where

$$\omega_r = \frac{\omega_{pi}}{\sqrt{1 + 4\pi \frac{\omega_{pe}^2}{k^2} \int_0^\infty f_0(v) dv}}.$$

Here, k is the ion-acoustic wave vector, and ω_{pe} and ω_{pi} are the electron and ion plasma frequencies respectively. This growth rate was found to be in agreement with the measured growth rates and as much as an order of magnitude lower than the growth rate from the Spitzer-Härm theory [38]

$$\gamma_e = \frac{\gamma_0 k \lambda_{De}}{(1 + k^2 \lambda_{De}^2)^2} \left[-1 + \frac{3}{2} \cos\theta \left(\frac{k v_{th}}{\omega_r} \right) \frac{\lambda_{ei}}{T_e} \frac{dT_e}{dr} \right] \qquad (2)$$

where $\gamma_0 = \sqrt{\pi/8}\, \omega_{pi}^2/\omega_{pe}$ and ω_r is calculated with a Maxwellian electron distribution function. Calculated growth rates used the measured plasma conditions and k vectors. As a result of the scattering geometry, including the finite size of the collection optic, and spatially varying plasma conditions the measured wave had $k\lambda_{De} = 0.4$–0.48 while calculations of the growth rate [γ, Eq. (1)] including collisions and ion Landau damping give a maximum growth rate at $k\lambda_{De} > 0.7$.

Figure 4(a) shows how the experimentally determined Knudsen number scaled with the radius, and indicates that the return current instability has a threshold of $\delta_T = 0.017 \pm 0.002$. The Knudsen number is within this range between r = 200 μm and r = 350 μm where the threshold was noted in Fig. 3(c). The Knudsen number (δ_T) is the scale parameter for the heat flux distribution function perturbation, and therefore the return current instability. It is the ratio of the mean free path to the temperature gradient scale length and therefore also an indicator of nonlocality. The mean free path and temperature gradient scale length were calculated from the profiles and individual points in Fig. 2(b).

An analytical threshold for the instability from Tikhonchuk *et al.* [31] is shown in green. The threshold

$$P = 1.5 \frac{v_{th}}{c_s} \frac{Z + 0.24}{Z + 4.2} \delta_T \qquad (3)$$

is based on the Spitzer-Härm theory with a correction to account for electron-electron collisions. A plasma is unstable to the return current instability when $P > 1$, which equates to a growth rate of $\gamma > 0$. The measured Knudsen number crosses the threshold [31] around 220 μm consistent with both the measured and simulated growth rates, indicating this model is a reliable estimate for the return current instability threshold. The threshold for the instability is also very close to the threshold for thermal transport nonlocality given by $\delta_T > 0.06/\sqrt{Z}$ [23], i.e., RCI will occur whenever the transport relations are nonlocal.

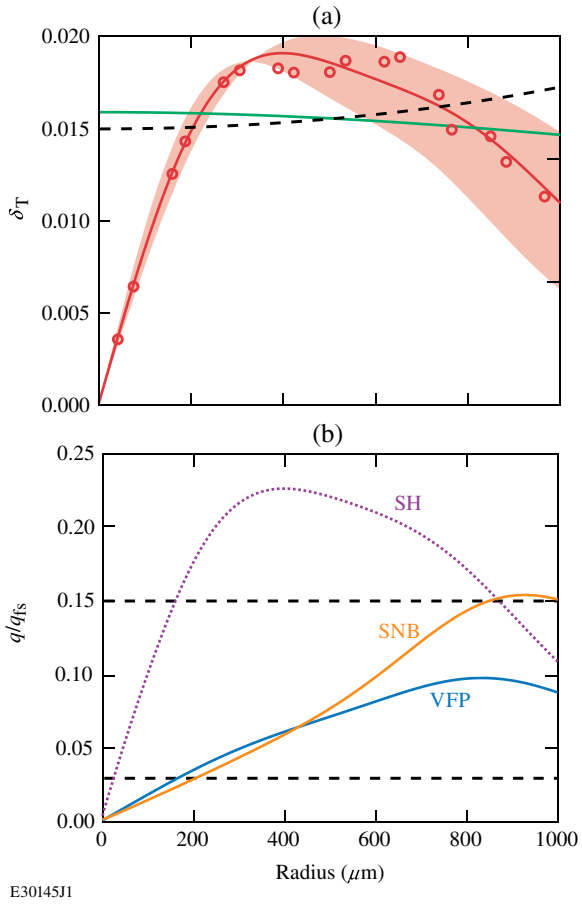

FIG. 4. (a) The Knudsen number calculated for individual data points (red circles) is compared with the hyperbolic tangent model (red curve) and its confidence interval (shaded region). A model from Tikhonchuk *et al.* [31] (green) is compared with the data while a nonlocality threshold is shown in black. (b) The heat flux is normalized to the free streaming limit for the Spitzer-Härm theory (purple), VFP simulations (blue), and the SNB model (orange). Two common flux limiters are shown in black.

Figure 4(b) shows the heat flux (q) normalized to the free streaming limit (q_{fs}). The heat flux from $K2$ is generally lower than Spitzer-Härm showing the nonlocal suppression. The Schurtz-Nicolaï-Busquet (SNB) model of nonlocal transport [24] shows the same heat flux suppression at smaller radii while other effects likely become dominant at higher radii. The heat flux from $K2$ also falls between the flux limiters of 0.03 and 0.15 that are frequently used to artificially reproduce nonlocal effects.

Heat transport is a ubiquitous process in plasma physics that is impacted by nonlocality and the instabilities it causes. This Letter has demonstrated the need to account for this nonlocality in the calculation of growth rates for instabilities involving ion-acoustic waves, such as the return current instability, and to account for the return current instability under conditions of nonlocal transport. Large spatial extends have been found for both the nonlocal transport and the return current instability. This can result in changes to instabilities and plasma conditions at a significant distance from the most unstable region. The threshold for the return current instability was found and is in good agreement with a simple temperature and density based model that can be used predictively in future work.

This material is based upon work supported by the Department of Energy National Nuclear Security Administration under Award No. DE-NA0003856, the Office of Fusion Energy Sciences under Award No. DE-SC0016253, the University of Rochester, and the New York State Energy Research and Development Authority. The work of M. S. was performed under the auspices of the U.S. Department of Energy by Lawrence Livermore National Laboratory under Contract No. DE-AC52-07NA27344. This document was prepared as an account of work sponsored by an agency of the United States government. Neither the United States government nor Lawrence Livermore National Security, LLC, nor any of their employees makes any warranty, expressed or implied, or assumes any legal liability or responsibility for the accuracy, completeness, or usefulness of any information, apparatus, product, or process disclosed, or represents that its use would not infringe privately owned rights. The views and opinions of authors expressed herein do not necessarily state or reflect those of the United States government or Lawrence Livermore National Security, LLC, and shall not be used for advertising or product endorsement purposes.

*Corresponding author.
milder@ualberta.ca

[1] R. S. Craxton *et al.*, Phys. Plasmas **22**, 110501 (2015).
[2] J. F. Drake, P. K. Kaw, Y. C. Lee, G. Schmidt, C. S. Liu, and M. N. Rosenbluth, Phys. Fluids **17**, 778 (1974).
[3] D. W. Forslund, J. Geophys. Res. **75**, 17 (1970).
[4] A. L. Milder, H. P. Le, M. Sherlock, P. Franke, J. Katz, S. T. Ivancic, J. L. Shaw, J. P. Palastro, A. M. Hansen, I. A. Begishev, W. Rozmus, and D. H. Froula, Phys. Rev. Lett. **124**, 025001 (2020).
[5] A. L. Milder, J. Katz, R. Boni, J. P. Palastro, M. Sherlock, W. Rozmus, and D. H. Froula, Phys. Rev. Lett. **127**, 015001 (2021).
[6] C. Zhang, C. K. Huang, K. A. Marsh, C. E. Clayton, W. B. Mori, and C. Joshi, Sci. Adv. **5**, eaax4545 (2019).
[7] B. Appelbe, M. Sherlock, O. El-Amiri, C. Walsh, and J. Chittenden, Phys. Plasmas **26**, 102704 (2019).
[8] M. Salewski, B. Geiger, A. S. Jacobsen, M. Garca-Muoz, W. W. Heidbrink, S. B. Korsholm, F. Leipold, J. Madsen, D. Moseev, S. K. Nielsen, J. Rasmussen, M. Stejner, G. Tardini, and M. Weiland, Nucl. Fusion **54**, 023005 (2014).
[9] S. Brunner and E. Valeo, Phys. Plasmas **9**, 923 (2002).
[10] A. R. Bell, R. G. Evans, and D. J. Nicholas, Phys. Rev. Lett. **46**, 243 (1981).
[11] V. Y. Bychenkov and W. Rozmus, Phys. Plasmas **22**, 082705 (2015).

[12] C. Bruulsema, W. A. Farmer, M. Sherlock, G. F. Swadling, M. D. Rosen, J. S. Ross, and W. Rozmus, Phys. Plasmas **29**, 012304 (2022).
[13] R. J. Henchen, M. Sherlock, W. Rozmus, J. Katz, D. Cao, J. P. Palastro, and D. H. Froula, Phys. Rev. Lett. **121**, 125001 (2018).
[14] D. Turnbull, A. Colatis, A. M. Hansen, A. L. Milder, J. P. Palastro, J. Katz, C. Dorrer, B. E. Kruschwitz, D. J. Strozzi, and D. H. Froula, Nat. Phys. **16**, 181 (2020).
[15] A. M. Hansen, K. L. Nguyen, D. Turnbull, B. J. Albright, R. K. Follett, R. Huff, J. Katz, D. Mastrosimone, A. L. Milder, L. Yin, J. P. Palastro, and D. H. Froula, Phys. Rev. Lett. **126**, 075002 (2021).
[16] J. S. Ross, H. S. Park, R. Berger, L. Divol, N. L. Kugland, W. Rozmus, D. Ryutov, and S. H. Glenzer, Phys. Rev. Lett. **110**, 145005 (2013).
[17] G. F. Swadling, C. Bruulsema, F. Fiuza, D. P. Higginson, C. M. Huntington, H. S. Park, B. B. Pollock, W. Rozmus, H. G. Rinderknecht, J. Katz, A. Birkel, and J. S. Ross, Phys. Rev. Lett. **124**, 215001 (2020).
[18] L. Spitzer and R. Härm, Phys. Rev. **89**, 977 (1953).
[19] S. I. Braginskii, in *Reviews of Plasma Physics*, edited by M. A. Leontovich (Consultants Bureau, New York, 1965), Vol. 1.
[20] J. F. Luciani, P. Mora, and J. Virmont, Phys. Rev. Lett. **51**, 1664 (1983).
[21] J. R. Albritton, E. A. Williams, I. B. Bernstein, and K. P. Swartz, Phys. Rev. Lett. **57**, 1887 (1986).
[22] E. M. Epperlein and R. W. Short, Phys. Fluids B **3**, 3092 (1991).
[23] V. Y. Bychenkov, W. Rozmus, V. T. Tikhonchuk, and A. V. Brantov, Phys. Rev. Lett. **75**, 4405 (1995).
[24] G. P. Schurtz, P. D. Nicolaï, and M. Busquet, Phys. Plasmas **7**, 4238 (2000).
[25] J. R. Albritton, Phys. Rev. Lett. **50**, 2078 (1983).
[26] J. P. Matte, T. W. Johnston, J. Delettrez, and R. L. McCrory, Phys. Rev. Lett. **53**, 1461 (1984).
[27] G. J. Rickard, A. R. Bell, and E. M. Epperlein, Phys. Rev. Lett. **62**, 2687 (1989).
[28] O. S. Jones, L. J. Suter, H. A. Scott, M. A. Barrios, W. A. Farmer, S. B. Hansen, D. A. Liedahl, C. W. Mauche, A. S. Moore, M. D. Rosen, J. D. Salmonson, D. J. Strozzi, C. A. Thomas, and D. P. Turnbull, Phys. Plasmas **24**, 056312 (2017).
[29] M. Rosen, H. Scott, D. Hinkel, E. Williams, D. Callahan, R. Town, L. Divol, P. Michel, W. Kruer, L. Suter, R. London, J. Harte, and G. Zimmerman, High Energy Density Phys. **7**, 180 (2011).
[30] S. D. Bale, M. Pulupa, C. Salem, C. H. Chen, and E. Quataert, Astrophys. J. Lett. **769**, L22 (2013).
[31] V. T. Tikhonchuk, W. Rozmus, V. Y. Bychenkov, C. E. Capjack, and E. Epperlein, Phys. Plasmas **2**, 4169 (1995).
[32] P. Monchicourt and P. A. Holstein, Phys. Fluids **23**, 1475 (1980).
[33] D. R. Gray and J. D. Kilkenny, Plasma Phys. **22**, 81 (1980).
[34] W. M. Manheimer, Phys. Fluids **20**, 265 (1977).
[35] S. H. Glenzer, W. Rozmus, V. Y. Bychenkov, J. D. Moody, J. Albritton, R. L. Berger, A. Brantov, M. E. Foord, B. J. MacGowan, R. K. Kirkwood, H. A. Baldis, and E. A. Williams, Phys. Rev. Lett. **88**, 235002 (2002).
[36] W. M. Manheimer, D. G. Colombant, and B. H. Ripin, Phys. Rev. Lett. **38**, 1135 (1977).
[37] W. Rozmus, A. V. Brantov, M. Sherlock, and V. Y. Bychenkov, Plasma Phys. Controlled Fusion **60**, 014004 (2018).
[38] A. V. Brantov, V. Y. Bychenkov, and W. Rozmus, Phys. Plasmas **8**, 3558 (2001).
[39] J. D. Moody, B. J. Macgowan, S. H. Glenzer, R. K. Kirkwood, W. L. Kruer, D. S. Montgomery, A. J. Schmitt, E. A. Williams, and G. F. Stone, Phys. Plasmas **7**, 2114 (2000).
[40] T. R. Boehly, R. S. Craxton, T. H. Hinterman, J. H. Kelly, T. J. Kessler, S. A. Kumpan, S. A. Letzring, R. L. McCrory, S. F. B. Morse, W. Seka, S. Skupsky, J. M. Soures, and C. P. Verdon, Rev. Sci. Instrum. **66**, 508 (1995).
[41] J. Katz, J. S. Ross, C. Sorce, and D. H. Froula, J. Instrum. **8**, C12009 (2013).
[42] J. Katz, R. Boni, C. Sorce, R. Follett, M. J. Shoup, and D. H. Froula, Rev. Sci. Instrum. **83**, 10E349 (2012).
[43] A. Visco, R. P. Drake, D. H. Froula, S. H. Glenzer, and B. B. Pollock, Rev. Sci. Instrum. **79**, 10F545 (2008).
[44] D. H. Froula, S. H. Glenzer, J. N. C. Luhmann, and J. Sheffield, *Plasma Scattering of Electromagnetic Radiation: Theory and Measurement Techniques*, 2nd ed. (Academic Press, New York, 2011).
[45] M. Sherlock, J. P. Brodrick, and C. P. Ridgers, Phys. Plasmas **24**, 082706 (2017).
[46] G. Bekefi, *Radiation Processes in Plasmas* (Wiley, New York, 1966).